Support and Size Effects of Activated Hydrotalcites for Precombustion CO$_2$ Capture

Niels N. A. H. Meis, Johannes H. Bitter, and Krijn P. de Jong*

Inorganic Chemistry and Catalysis, Department of Chemistry, Debye Institute for Nanomaterials Science, Utrecht University, P.O. Box 80 083, 3508 TB Utrecht, The Netherlands

A series of Mg–Al hydrotalcites (HTs) with lateral platelet sizes ranging from 40 nm to 2 μm were prepared hydrothermally. Small HT platelets (~20 nm) were obtained by deposition onto a carbon nanofiber (CNF) support. The CO$_2$ sorption capacity at 523 K for the activated unsupported HT was low (~0.1 mmol·g^{-1}), regardless of the platelet size of the HT precursor. In addition, no relation was found between the CO$_2$ sorption properties of activated HTs and their specific surface area. The sorption capacity of the activated CNF-supported HTs was increased, depending on the HT loading, by an order of magnitude (1.3–2.5 mmol·g$_{HT}$$^{-1}$) compared to that of the activated unsupported HT. We propose that the CO$_2$ sorption capacities of HTs are determined by the amounts of low-coordination oxygen sites in the Mg(Al)O$_x$ nanoparticles, which is highest on supported HTs.

1. Introduction

Carbon capture and storage (CCS) is an option to decrease the vast amounts of CO$_2$ (28 Gt in 2005[1]) released into the atmosphere through fossil fuel utilization.[2] CO$_2$ capture can be divided in two classes. The first of theses is end-of-pipe capture, for example, at power plants; this is the so-called postcombustion capture. Alternatively, CO$_2$ affiliated with the production of hydrogen, for example, through the water–gas shift reaction (WGSR: CO + H$_2$O $\leftrightarrow$ CO$_2$ + H$_2$) can be captured, preventing the release of CO$_2$ and driving the equilibrium of the reaction to the hydrogen side; this is one of the options for precombustion capture. For postcombustion capture, the amines used commercially are corrosive, so special reactor materials are needed.[3] Alternatives based on solid sorbents involve modified SBA15[4–6] and MCM41 amines,[4,5] metal–organic frameworks (MOFs),[7–10] and zeolitic imidazolate frameworks (ZIFs).[11,12] For precombustion capture, high temperatures (>250 °C) are required. Most of the studied materials, such as lithium zirconates,[13–16] sodium zirconates,[17,18] CaO,[19–21] basic alumina,[22] and carbon-based adsorbents,[23–25] do not meet the required properties with respect to sorption capacities, kinetics, and mechanical strength. Optimal sorbents for precombustion use should display properties such as selectivity toward CO$_2$, a high adsorption capacity at high temperatures (>523 K), adequate adsorption and desorption kinetics at operating conditions (facile regeneration), long-term stability upon cyclic use, adequate mechanical strength, and low costs. A number of solid basic oxides, especially hydrotalcites, are promising as reusable sorbent.[26–29] Hydrotalcites (HTs) belong to the class of anionic clay minerals also known as layered double hydroxides. The structure of HTs closely resembles that of brucite, Mg(OH)$_2$, where Mg^{2+} is octahedrally coordinated by hydroxyl groups. These octahedra share adjacent edges to form sheets or layers. In HTs, some of the Mg^{2+} ions are replaced by Al^{3+} ions. This results in positively charged layers, which are balanced by charge-compensating anions (e.g., Cl$^-$, Br$^-$, CO$_3$$^{2-}$, I$^-$, NO$_3$$^-$, OH$^-$, SO$_4$$^{2-}$) located in the interlayer region, where hydrating water molecules are also accommodated. HTs have received considerable attention in recent years because of their wide range of applications, such as base

catalysts,[30–34] ion exchangers,[35,36] polymer stabilizers, and drug targets.[37] The edges, and thus the lateral dimensions of the HTs, have a significant influence on their catalytic behavior.[30,32,38] Previous work from our group[30] showed an increase in activity in base catalysis with decreasing platelet size for activated HTs (self-condensation of acetone). It was concluded that only the basic sites at the edges of the hydrotalcite platelets were involved in this low-temperature reaction (273 K). In this work, we report on the structure–activity relationship of the Mg–Al hydrotalcite platelet size before activation and the textural properties of the activated materials with their CO$_2$ capture properties. The samples were characterized using X-ray diffraction (XRD), scanning electron microscopy (SEM), transmission electron microscopy (TEM), and nitrogen physisorption.

2. Experimental Section

2.1. Preparation of Unsupported Hydrotalcites. To an aqueous solution (150 mL) containing 0.7 mol of NaOH and 0.09 mol of Na$_2$CO$_3$ was added dropwise an aqueous solution (70 mL) of 0.1 mol of Mg(NO$_3$)$_2$·6H$_2$O and 0.05 mol of Al(NO$_3$)$_3$·9H$_2$O. The resulting white suspension was aged at 298 K for 24 h under vigorous stirring. Subsequently, the suspension was filtered and washed extensively with demineralized water. The sample, further denoted as HT$_{298}$, was dried for 24 h at 393 K. To increase the crystallite size of the HT, the aging was also performed at 313, 333, and 353 K. These as-synthesized samples are further denoted as HT$_{313}$, HT$_{333}$, and HT$_{353}$. Aging at higher temperatures (i.e., 373, 393, 413, and 433 K) was performed in an autoclave. The synthesis mixture of NaOH, Na$_2$CO$_3$, Mg(NO$_3$)$_2$·6H$_2$O, and Al(NO$_3$)$_3$·9H$_2$O as described above was first stirred for 1 h at room temperature. Next, the precipitate was poured into a Teflon holder, which was placed into a stainless steel rotating autoclave, where the sample was aged for 16 h at the desired temperature. Subsequently, the suspension was filtered, washed extensively with demineralized water, and dried for 24 h at 393 K. These as-synthesized samples are further denoted as HT$_{373}$, HT$_{393}$, HT$_{413}$, and HT$_{433}$.

Preparation of Hydrotalcites Using the Urea Procedure.[39] An aqueous solution (150 mL) of 0.1 mol of Mg(NO$_3$)$_2$·6H$_2$O, 0.05 mol of Al(NO$_3$)$_3$·9H$_2$O, and 0.75 mol of urea was

* To whom correspondence should be addressed. E-mail: K.P.dejong@uu.nl.

vigorously stirred and heated at 363 K and kept at this temperature for 24 h. The pH increased from 3.0 to ~9.0 at the end of the reaction. The resulting white suspension was filtered, washed extensively with demineralized water, and dried at 393 K for 24 h. This as-synthesized sample is further denoted as HT_{urea}.

2.2. Preparation of Supported Hydrotalcites. Carbon Nanofiber Growth. A silica-supported nickel catalyst with a metal loading of 20 wt % was prepared by deposition precipitation using the hydrolysis of urea at 363 K.[40] Silica (8.5 g), nickel nitrate (10.6 g), and urea (7.9 g) were suspended in 1 L of demineralized water and vigorously stirred. The reaction mixture was heated at 363 K and kept at this temperature for 16 h. The resulting green suspension was filtered, washed extensively with demineralized water, and dried at 393 K for 24 h. A sieve fraction of 425−850 μm of the catalyst precursor was calcined in static air at 873 K (5 K·min^{-1}) for 3 h. Next, the Ni catalyst precursor (5.0 g) was reduced in situ at 973 K in a fixed-bed reactor for 2 h in a 30% H$_2$/N$_2$ flow (800 mL·min^{-1}). After the temperature had been decreased to 823 K, synthesis gas (33% CO/13% H$_2$) balanced with N$_2$ was passed through the reactor for 24 h at a pressure of 2 bar in a total flow of 800 mL·min^{-1}. Removal of the growth catalyst and oxidation of the carbon nanofiber (CNF) was performed as reported in the literature[41,42] using subsequent treatments in aqueous 1 M KOH and concentrated HNO$_3$.

CNF-Supported Hydrotalcites. To prepare supported Mg−Al hydrotalcites [Mg/Al = 2, (at/at)], 5.0 g of CNF was impregnated in a 250-mL round-bottom flask with a solution containing 3.3 mL of Mg(NO$_3$)$_2$ (1.4 M) and Al(NO$_3$)$_3$ (0.7 M). After this mixture had been dried for 1 h at 393 K, a solution of 3.0 mL NaOH (8.3 M) and Na$_2$CO$_3$ (0.56 M) was added. Aging was performed in a water-saturated atmosphere under a nitrogen flow (7 mL·min^{-1}) for 16 h at 333 K and was followed by extensive washing with demineralized water and drying at 393 K for 24 h. This as-synthesized sample is denoted as HT_{10}-CNF, with the number 10 referring to the weight loading (%) of HT deposited on CNF. The reported nominal weight loadings are close to the actual loadings, as reported earlier.[32] A second sample was prepared as described above with a solution containing 3.3 mL of Mg(NO$_3$)$_2$ (0.7 M) and Al(NO$_3$)$_3$ (0.35 M). This as-synthesized sample is denoted as HT_5-CNF. A third sample was prepared as described above. After that, the synthesis procedure was repeated once. This as-synthesized sample is denoted as HT_{18}-CNF. General supported samples will be referred to as HT-CNF.

2.3. Characterization. Powder X-ray diffraction (XRD) patterns were measured using a Bruker-AXS D8 advance powder diffraction apparatus equipped with an automatic divergence slit (filtered Co K$_\alpha$ radiation, λ = 1.79026 Å). N$_2$ physisorption measurements were performed using a Micromeritics Tristar 3000 analyzer after the samples had been dried at 393 K in a vacuum for at least 20 h prior to the measurements; pore volume was measured at at P/P_0 = 0.995. CO$_2$-loaded samples (HT_{act-CO_2}) for nitrogen physisorption were cooled to room temperature after the adsorption step (vide infra). SEM micrographs were obtained using a Philips XL30FEG electron microscope equipped with an energy-dispersive X-ray (EDX) detector for elemental analysis. TEM micrographs were obtained with an FEI Technai 20 FEG instrument equipped with an EDX detector operating at 200 kV. TEM samples were dispersed on a holey carbon film supported on a copper grid. A Branson 450-W Sonifier was used for ultrasonic treatment for 1 h at 323 K.

Table 1. Experimental Conditions for Sorption Measurements with 2 g of HT$_{T-act}$ or 5 g of HT$_{act}$-CNF

	flow (mL·min^{-1})	composition	temp (K)
activation	30	100% N$_2$	323−773 (5 K·min^{-1}, 1 h)
adsorption	30	83% N$_2$/12% H$_2$O/5% CO$_2$	523 (max 30 min)
desorption	30	100% N$_2$	523−773 (5 K·min^{-1}, 1 h)

2.4. CO$_2$ Sorption Measurements. CO$_2$ sorption measurements were performed in a quartz plug-flow reactor with an inner diameter of 12 mm. The gas flows (N$_2$, CO$_2$) were passed in downflow mode through the reactor and controlled by mass flow controllers (Brooks 5850s). The total pressure in the setup was maintained at 1.10 bar, using a backpressure controller (Brooks 5866). A tubular oven was placed around the reactor to control the process temperature. The reactor was loaded with 2.0 g of sample (bed height = 35 mm) using a sieve fraction with particle sizes of 212−500 μm. For HT-CNF, the reactor was loaded with 5 g of sample (bed height = 85 mm), which contained 0.25, 0.5, or 1.0 g of HT. All samples were activated by heating in N$_2$ (30 mL·min^{-1}) at 773 K (5 K·min^{-1}) for 1 h to remove CO$_2$ and water from the starting material (HT$_{act}$, activation step). The activated samples are denoted as HT$_{T-act}$ and HT$_{act}$-CNF, where T is the synthesis temperature in Kelvin and act refers to the activation step. After activation, all samples were subjected to at least two identical adsorption (523 K) and desorption (773 K) cycles to assess reproducibility. Conditions for the adsorption and desorption steps are given in Table 1. The total flow throughout all experiments was 30 mL·min^{-1}. N$_2$ was humidified with CO$_2$-free water using a saturator set at 331 K. All adsorption experiments were performed for 30 min in 5% CO$_2$. After adsorption, the system was flushed with N$_2$. Desorption was performed by heat treatment in dry nitrogen (30 mL·min^{-1}) at 773 K (5 K·min^{-1}) for 1 h. To prevent gasification of the CNF support material at higher temperatures in steam, dry nitrogen was used during desorption in all measurements to obtain comparable results between HT$_{T-act}$ and HT$_{act}$-CNF samples. Blank measurements were performed with either a nonadsorbing material (SiC) or CNF, with the same particle size range and bed volume as the HT-containing material. There was no CO$_2$ adsorption by the supports. The effluent gas was analyzed by online FT-IR spectroscopy using a Midac corporation 2000 M series instrument. For each spectrum, eight scans were accumulated with a resolution of 4 cm^{-1}; spectra were recorded every 13 s. The IR cell, made of stainless steel, had a path length of 2 mm and contained CaF$_2$ windows. The sample compartment was continuously purged with a stream of dry N$_2$ to prevent interference of CO$_2$ present in the atmosphere. A background spectrum using an empty cell was acquired prior to sorption measurements. The integrated area from 2280 to 2390 cm^{-1} was used to quantify the amount of CO$_2$ in the gas phase. A CO$_2$ concentration above 100 ppm is defined as breakthrough. From the breakthrough time and the flow and concentration, the amount of CO$_2$ was calculated.

3. Results and Discussion

3.1. Characterization of Materials. To establish the crystallographic ordering and purity of the as-synthesized HT samples, XRD analysis was performed. Figure 1 shows selected XRD patterns of unsupported as-synthesized HTs (HT$_{298}$, HT$_{333}$, HT$_{373}$, HT$_{433}$, and HT$_{urea}$). The signals at $2\theta \approx 13.5°$, 27.6°, and 40.0°, corresponding to the (003), (006), and (009/012) crystal planes, respectively, indicate well-formed crystalline layered structures. In addition, at high synthesis temperatures,
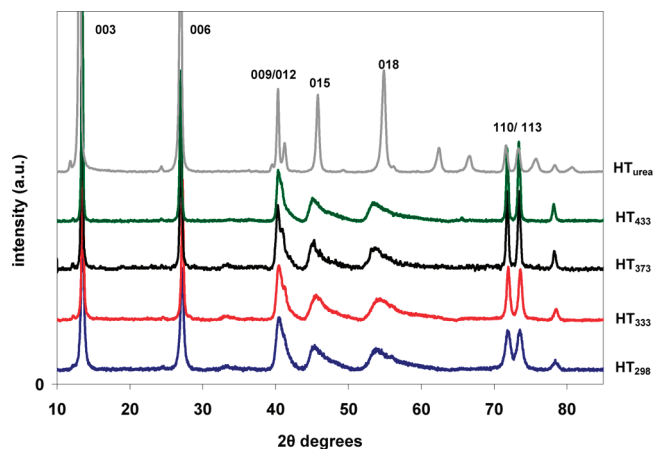
Figure 1. Selected XRD profiles of as-synthesized HT$_{298}$, HT$_{333}$, HT$_{373}$, HT$_{433}$, and HT$_{urea}$.
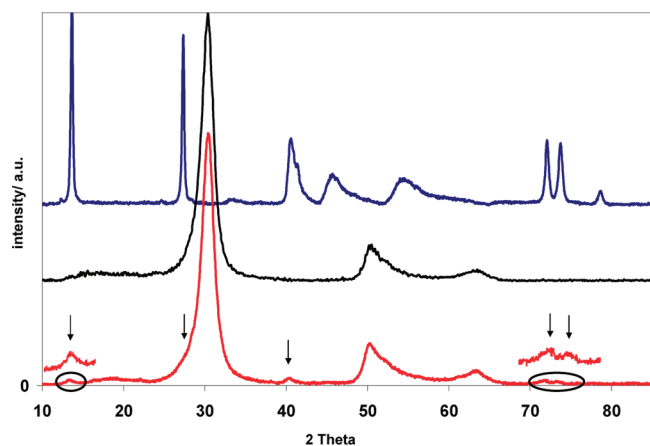

Figure 2. XRD profiles of as-synthesized HT$_{333}$, CNF, and HT$_{10}$-CNF. Arrows indicate HT peaks.

signals were detected close to the (003) and (006) signals (11.3° and 24.6°), which can be ascribed to diffractions caused by Kβ radiation. For all samples except HT$_{urea}$, the signals were representative of HTs with interlayer carbonate. In contrast, HT$_{urea}$ showed signals at 62.9° and 67.1° that are characteristic for a sample with hydroxylic ions (OH$^-$) in the interlayer.[43] Because the decomposition of urea takes place at relatively low pH (pH ∼6), the (bi)carbonate concentration in the solution will be low, and hydroxyl ions (OH$^-$) in the interlayer are favored. To summarize, only crystalline hydrotalcites were detected by XRD, indicating the high purity of all samples. The selected XRD pattern of the supported hydrotalcite (HT$_{10}$-CNF) is compared to those of HT$_{333}$ and to pure CNF in Figure 2. In the supported sample, diffraction lines due to the presence of HT, as indicated by the arrows, can be distinguished next to the strong lines of the CNF support. From this figure, it is clear that the diffraction lines of hydrotalcite in the supported sample are broader than those of unsupported HT, which implies that the HT crystallites on the supported sample (HT$_{10}$-CNF) are smaller and/or less ordered.[44] In addition, the intensity of the signals for supported HT is much smaller than that for the unsupported HT sample, after identical counting times, as a result of the small HT platelets[31] and/or lower amount of HT present.

The particle size and morphology of unsupported HT samples were analyzed by SEM, whereas the supported HTs were analyzed by TEM. Figure 3 shows SEM micrographs of selected hydrotalcites (HT$_{313}$, HT$_{373}$, HT$_{473}$, and HT$_{urea}$). Samples pre-
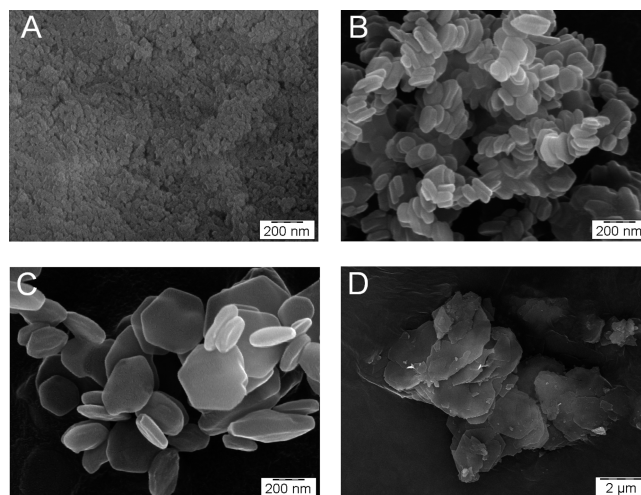
Figure 3. SEM micrographs of (A) HT$_{313}$, (B) HT$_{373}$, (C) HT$_{433}$, (D) HT$_{urea}$.
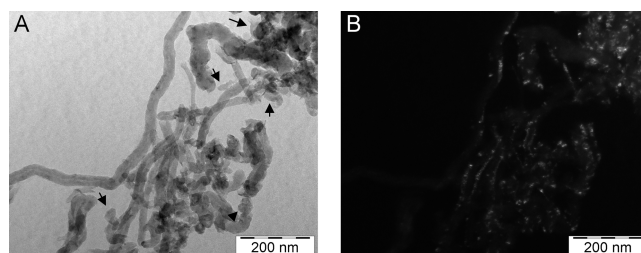

Figure 4. TEM micrographs of HT$_{10}$-CNF in (A) bright field (arrows indicate HT platelets) and (B) dark field (small HT crystallites are visible).

pared using NaOH/Na$_2$CO$_3$ as a base (Figure 3A–C) showed regular hexagonally shaped HT platelets. The micrographs highlight the difference in lateral platelet size due to the aging temperature, with an increase in size occurring with increasing temperature. When urea was used as the precipitant, very large HT platelets (2 μm, Figure 3D) were obtained, in line with literature reports.[39,45] Figure 4 shows selected bright- and dark-field TEM micrographs of HT$_{10}$-CNF. In bright-field mode, HTs are difficult to distinguish from carbon, because of a similarity in density. In dark-field mode (i.e., diffraction contrast imaging), the small HT crystallites were easier to observe (Figure 4). The dark-field micrographs revealed more HTs than could be detected in bright-field mode. For clarity, the arrows in Figure 4A indicate some of the HT platelets.

An overview of the average lateral platelet sizes as a function of the aging temperature, based on SEM and TEM measurements to determine the platelet sizes of 30 individual HT platelets, is shown in Figure 5. Clearly, unsupported as-synthesized HT samples showed an increase in lateral platelet size with increasing synthesis temperature. The average crystalline platelets increased from 35 nm (HT$_{298}$) to 300 nm (HT$_{433}$). HT$_{urea}$ had the largest lateral platelet size (2 μm), whereas supported hydrotalcites displayed the smallest crystalline platelets (∼20 nm). In conclusion, the HT platelets were tuned from 20 nm to 2 μm, and all HT precursor samples showed good crystallinity.

3.2. CO$_2$ Adsorption and Desorption Kinetics. Prior to sorption measurements, all samples were activated at 773 K in N$_2$. Representative breakthrough curves for CO$_2$ adsorption at 523 K on these activated HTs are shown in Figure 6a. Note that, after activation, the hydrotalcite material still retained its mesoscopic shape (i.e., the platelets were still present), but XRD
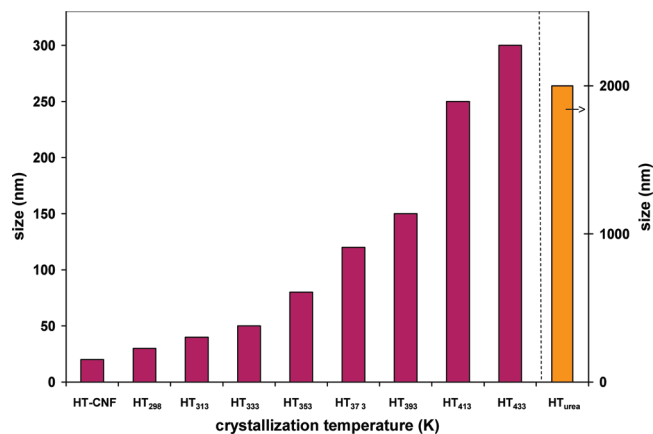
Figure 5. Effect of average platelet size on crystallization temperature of as-synthesized HTs.
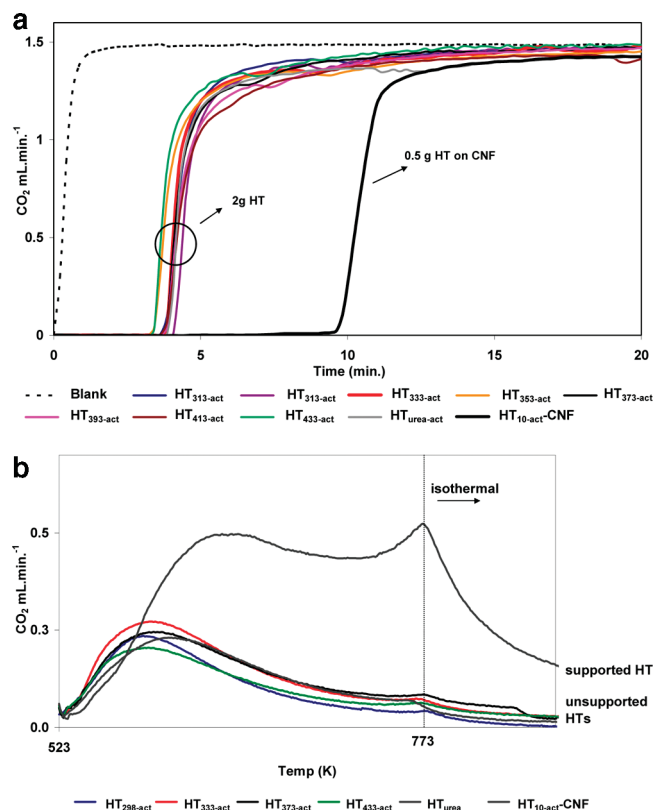

Figure 6. (a) Representative breakthrough curves of activated HTs (2 g) and activated HT$_{10}$-CNF (5 g) (flow: 25 mL·min^{-1} N$_2$, 3.5 mL·min^{-1} H$_2$O, and 1.5 mL·min^{-1} CO$_2$ at 523 K). (b) Selected representative desorption profiles of activated HTs and activated HT$_{10}$-CNF (flow: 30 mL·min^{-1} N$_2$, 523−773 K, 1 h).

revealed broad Mg(Al)O$_x$ diffractions. The activated samples are denoted as HT$_{act}$ and HT$_{act}$-CNF, where the subscript "act" denotes the activated material [Mg(Al)O$_x$] after heat treatment. All activated unsupported HTs showed, within experimental error, the same breakthrough times, which corresponded to a CO$_2$ capacity of approximately 0.1 mmol·g^{-1}, irrespective of the original platelet size. For the supported activated HTs, the breakthrough times were significantly longer (Figure 6a). Even though these samples contained only 5, 10, and 18 wt % HT, breakthrough times were 10.1 min for HT$_{5-act}$-CNF, 9.5 min for HT$_{10-act}$-CNF (shown), and 13.0 min for HT$_{18-act}$-CNF, which correspond to capacities of 2.5, 1.3, and 1.7 mmol·g$_{HT}$$^{-1}$, that is, an order of magnitude higher compared to those for the activated unsupported HTs. A selected number of desorption
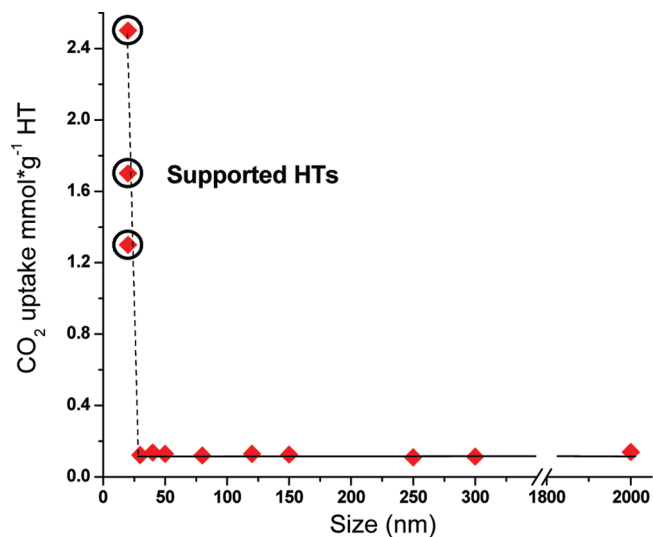

Figure 7. CO$_2$ capacities at 523 K of all activated (supported) HTs and their laterals sizes. The supported samples have a 10−25-fold higher capacities than the unsupported samples.
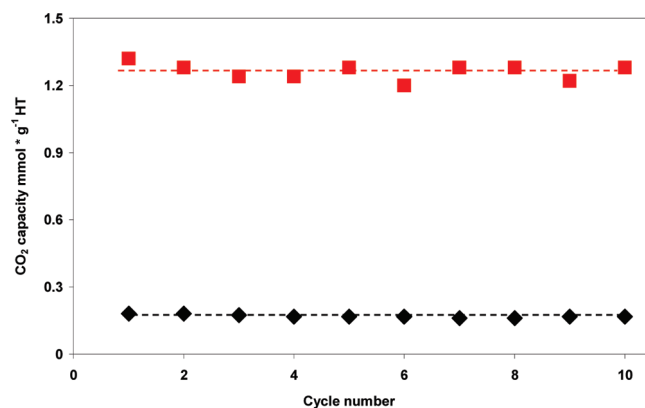

Figure 8. CO$_2$ capacity as function of adsorption−desorption cycles for two selected samples: unsupported HT$_{333-act}$ (♦) and HT$_{10-act}$-CNF (■).

profiles are shown in Figure 6b. Under these dry conditions, all activated unsupported HTs exhibited similar desorption characteristics. Desorption of the activated supported sample started at a higher temperature compared to that of the activated unsupported HT, and the first desorption maximum of HT$_{10-act}$-CNF occurred at 580 K. These details point to stronger bonding of adsorbed CO$_2$. The high-temperature desorption peak (773 K) is more pronounced with HT-CNF, which is more likely related to absorption. Note that the presence of steam during desorption will most likely negatively affect the cycle stability of the CNF-supported materials.

Figure 7 summarizes the adsorption capacity at 532 K of all samples as a function of their original HT platelet size. Unsupported hydrotalcites (platelet size between 30 nm and 2 μm) evidently all have an invariant adsorption capacity (∼0.1 mmol·g^{-1}). Lemonidou et al.[20] also reported that the CO$_2$ capacity did not depend on size for CaO-based materials. However, their materials had sizes in the range of 1−10 μm, whereas our precursor samples had sizes from 35 nm to 2 μm. Surprisingly, the supported HT samples with a platelet size of ∼20 nm had much higher capacities, depending on the HT loading, of 1.3−2.5 mmol·g$_{HT}$$^{-1}$. Figure 8 shows the CO$_2$ sorption capacities of HT$_{333-act}$ and HT$_{10-act}$-CNF as a function of the number of adsorption−desorption cycles. Clearly, the materials showed stable behavior.

Table 2. Physicochemical Properties of the Hydrotalcites HT_{as}, HT_{act}, and HT_{act-CO_2}

	HT_{as}		HT_{act}		HT_{act-CO_2}	
sample	S_{BET} $(m^2 \cdot g^{-1})$	V_{tot} $(cm^3 \cdot g^{-1})$	S_{BET} $(m^2 \cdot g^{-1})$	V_{tot} $(cm^3 \cdot g^{-1})$	S_{BET} $(m^2 \cdot g^{-1})$	V_{tot} $(cm^3 \cdot g^{-1})$
HT_{298}	100	0.6	262	0.86	126	0.27
HT_{313}	93	0.67	125	0.74	216	0.57
HT_{333}	53	0.35	68	0.46	117	0.41
HT_{353}	47	0.4	83	0.45	50	0.44
HT_{373}	24	0.11	68	0.16	127	0.44
HT_{393}	21	0.09	209	0.22	23	0.14
HT_{413}	19	0.07	157	0.17	172	0.18
HT_{433}	15	0.07	183	0.17	139	0.2
HT_{urea}	32	0.1	245	0.26	72	0.2
HT_{333-us}					211	0.77
CNF	155	0.34				
HT_5-CNF	107	0.29	124	0.31	–	–
HT_{10}-CNF	97	0.19	114	0.22	110	0.23
HT_{18}-CNF	98	0.18	105	0.20	–	–

Because no relation could be found between platelet size and capacity, we investigated whether CO_2 capture properties of the HTs were related to their textural properties, especially after activation (Table 2). In Table 2, some physicochemical properties of the unsupported HTs are listed. Micropores were not, or were hardly, present in the samples. The surface area of the as-synthesized HTs (HT_{as}) varied from 15 to 100 $m^2 \cdot g^{-1}$ and decreased with increasing platelet size (i.e., with increasing aging temperature), which is in good agreement with the literature.[46] Activation (meaning heat treatment in N_2 at 773 K; see section 2.3) of the HTs (HT_{act}) resulted in an increase in surface area and pore volume. To investigate how the textural properties of activated HTs changed after CO_2 loading, nitrogen physisorption experiments were also performed on the CO_2-loaded samples (Table 2, HT_{act-CO_2}; see 2.4). All loaded samples showed a decrease in pore volume compared to that of activated HT, with the exception of HT_{373-act-CO_2}. After CO_2 loading, the surface areas of samples HT_{298}, HT_{333}, HT_{373}, and HT_{433} were in a similar range (117−129 $m^2 \cdot g^{-1}$), whereas the surface areas of the other loaded samples (HT_{313}, HT_{353}, HT_{393}, HT_{413}, and HT_{urea}) varied significantly. Moreover, after being loaded with CO_2, five samples decreased in surface area (HT_{298}, HT_{353}, HT_{393}, HT_{433}, and HT_{urea}), whereas the other four samples (HT_{313}, HT_{333}, HT_{373}, and HT_{413}) exhibited an increase in surface area. Thus, both the activated HTs and the CO_2-loaded samples showed nonsystematic variations of surface area and pore volume. These results indicate that there is no relation between CO_2 capacity and textural properties, which is in agreement with the results of Kim and co-workers.[47] The pore volumes and surface areas of the CNF-supported HTs were significantly lower than the corresponding values for CNF, which indicates a partial filling of the pores with HT (Table 2, bottom). The surface areas and pore volumes of activated supported HTs were slightly higher than those of their precursors.

As discussed above, the CO_2 sorption capacity of activated unsupported HTs was found to be invariant with the surface area. Therefore, the coverage of CO_2 per square nanometer must increase with decreasing surface area (see Figure 9). Now, we attempt to explain this observation. For MgO, which has a structure similar to that of the activated HTs, the sites for CO_2 adsorption are expected to associate with low-coordinated $O^{2-}-Mg^{2+}$ sites.[48−58] In other words, the C of CO_2 adsorbs on low-coordinated oxygen (oxygen surrounded by fewer than five atoms). We propose that the active sites for CO_2 adsorption on activated HTs are also associated with $O^{2-}-Mg^{2+}$ sites (MgO + CO_2 ↔ $MgCO_3$). During CO_2 sorption, the acidic CO_2 reacts with basic O^{2-} sites depending on their coordination. Oxygen atoms located at edges and corners of the crystal planes have
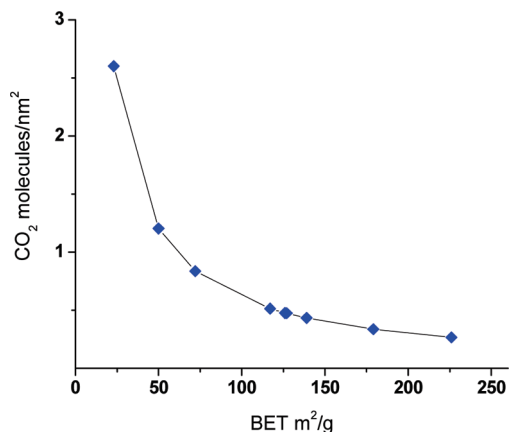
Figure 9. Effect of surface area on activated unsupported HTs: coverage of CO_2 increases with decreasing surface area.
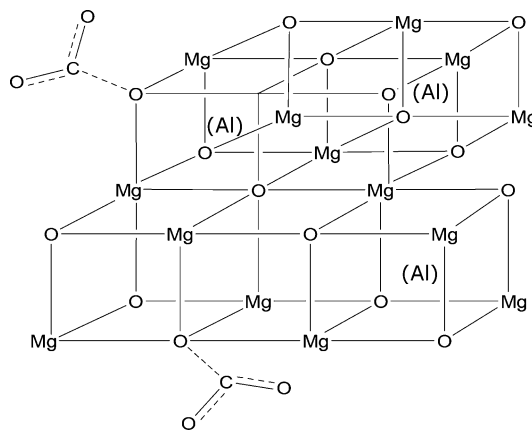
Figure 10. Corners and edges are important for CO_2 adsorption.

stronger basicity than oxygen atoms in basal planes. Therefore, the energy level of surface oxygen increases with decreasing coordination number. The interactions are assumed to be mainly of the highest occupied molecular orbital (HOMO)−lowest unoccupied molecular orbital (LUMO) type.[53] Consequently, the HOMO−LUMO energy gap between O^{2-} and CO_2 is reduced on corners and edges (under coordination of oxygen), and thus, charge transfer from O^{2-} to CO_2 will occur. Therefore, the interaction from an edge or corner O^{2-} anion with a CO_2 molecule can lead to surface carbonate species.[59,60] For MgO surfaces, Pettersson et al.[59,60] calculated energetically favorable interactions with CO_2. They concluded that, on a regular unperturbed MgO(100) surface, no CO_2 adsorption occurs. However, three- and four-coordinated O^{2-} edges and corners (O_{3c}, O_{4c}) showed a reduction in the HOMO−LUMO energy gap. Consequently, adsorption with CO_2 on an edge or corner is more likely to occur (Figure 10), which illustrates our proposal. As a result of these findings, we propose that the amounts of low-coordinated oxygen in our activated unsupported samples are identical on a weight basis for all samples. After activation, the samples lose their original crystalline platelet structure and are all Mg(Al)O_x-like, although the platelet shapes of the HTs, as visualized by SEM, remain. Apparently, larger Mg(Al)O_x particles contain more surface defects per unit surface area and, consequently, higher coverages of CO_2 (Figure 10). We propose that the high increase in CO_2 capacities of the activated supported HTs is based on a greater number of defects on the small Mg(Al)O_x crystals. The individual crystals are anchored on the CNF and thus have less flexibility, which might contribute to more defects and low-coordinated oxygen. In other

words, more adsorption sites are formed in the activated supported HTs [Mg(Al)O$_x$] upon heat treatment, as result of the limited mobility. Apparently, for unsupported materials, the total numbers of adsorption sites in the reactor are similar for all samples, because the adsorption capacity is the same for all samples (Figure 6a). We speculate that the number of defects per surface area is larger for larger particles (i.e., those formed from larger HT platelets) than for the smaller particles, probably as a result of a more difficult annealing (i.e., lower mobility of ions) in larger particles during activation. Additional evidence for the role of low-coordination sites comes from the use of an unsupported ultrasonic-treated HT sample (data not shown). Sonication is expected to create defects on the surface/edges of the HT.[61,62] Indeed, the capacity of a sonicated sample increased to 0.2 mmol·g^{-1} as compared to the 0.1 mmol·g^{-1} for a regular sample. Unfortunately, after the first cycle, the capacity of the sonicated sample dropped to the original value of the regular HTs.

4. Conclusions

In this article, we have presented a study of CO$_2$ sorption measurements at 523 K on Mg–Al hydrotalcites with lateral platelet sizes from 20 nm to 2 μm. Unsupported hydrotalcites showed an invariant and low capacity as a function of platelet size. An increase by a factor 10–25 in HT-weight-based capacities was accomplished by supporting the HTs on CNF. Nitrogen physisorption measurements showed no dependence of CO$_2$ capacity and specific surface area for the unsupported HT. Currently, we tentatively relate the higher capacity of the activated supported samples to a higher density of low-coordination oxygen (edges and corners) in the Mg(Al)O$_x$-phase crystal interacting with the CNF surface.

Literature Cited

(1) Intergovernmental Panel on Climate Change (IPCC). *Climate Change 2007: The Physical Science Basis*; Cambridge University Press: Cambridge, U.K., 2007.

(2) The CATO-2 Project. http://CO2-cato.nl/.

(3) Fauth, D. J.; Frommell, E. A.; Hoffman, J. S.; Reasbeck, R. P.; Pennline, H. W. Eutectic salt promoted lithium zirconate: Novel high temperature sorbent for CO$_2$ capture. *Fuel Process. Technol.* **2005**, *86* (14–15), 1503–1521.

(4) Hicks, J. C.; Drese, J. H.; Fauth, D. J.; Gray, M. L.; Qi, G. G.; Jones, C. W. Designing adsorbents for CO$_2$ capture from flue gas-hyperbranched aminosilicas capable,of capturing CO$_2$ reversibly. *J. Am. Chem. Soc.* **2008**, *130* (10), 2902–2903.

(5) Yue, M. B.; Sun, L. B.; Cao, Y.; Wang, Y.; Wang, Z. J.; Zhu, J. H. Efficient CO$_2$ capturer derived from as-synthesized MCM-41 modified with amine. *Chem.–Eur. J.* **2008**, *14* (11), 3442–3451.

(6) Wang, X.; Schwartz, V.; Clark, J. C.; Ma, X.; Overbury, S. H.; Xu, X.; Song, C. Infrared Study of CO$_2$ Sorption over "Molecular Basket" Sorbent Consisting of Polyethylenimine-Modified Mesoporous Molecular Sieve. *J. Phys. Chem. C* **2009**, *113* (17), 7260–7268.

(7) Babarao, R.; Jiang, J. W. Molecular screening of metal–organic frameworks for CO$_2$ storage. *Langmuir* **2008**, *24* (12), 6270–6278.

(8) Llewellyn, P. L.; Bourrelly, S.; Serre, C.; Vimont, A.; Daturi, M.; Hamon, L.; De Weireld, G.; Chang, J. S.; Hong, D. Y.; Hwang, Y. K.;

Jhung, S. H.; Ferey, G. High uptakes of CO$_2$ and CH$_4$ in mesoporous metal–organic frameworks MIL-100 and MIL-101. *Langmuir* **2008**, *24* (14), 7245–7250.

(9) Finsy, V.; Ma, L.; Alaerts, L.; De Vos, D. E.; Baron, G. V.; Denayer, J. F. M. Separation of CO$_2$/CH$_4$ mixtures with the MIL-53(Al) metal–organic framework. *Microporous Mesoporous Mater.* **2009**, *120* (3), 221–227.

(10) Yazaydin, A. O. z. r.; Benin, A. I.; Faheem, S. A.; Jakubczak, P.; Low, J. J.; Willis, R. R.; Snurr, R. Q. Enhanced CO$_2$ Adsorption in Metal–Organic Frameworks via Occupation of Open-Metal Sites by Coordinated Water Molecules. *Chem. Mater.* **2009**, *21* (8), 1425–1430.

(11) Banerjee, R.; Phan, A.; Wang, B.; Knobler, C.; Furukawa, H.; O'Keeffe, M.; Yaghi, O. M. High-throughput synthesis of zeolitic imidazolate frameworks and application to CO$_2$ capture. *Science* **2008**, *319* (5865), 939–943.

(12) Liu, D. H.; Zheng, C. C.; Yang, Q. Y.; Zhong, C. L. Understanding the Adsorption and Diffusion of Carbon Dioxide in Zeolitic Imidazolate Frameworks: A Molecular Simulation Study. *J. Phys. Chem. C* **2009**, *113* (12), 5004–5009.

(13) Ida, J.; Lin, Y. S. Mechanism of high-temperature CO$_2$ sorption on lithium zirconate. *Environ. Sci. Technol.* **2003**, *37* (9), 1999–2004.

(14) Pfeiffer, H.; Knowles, K. M. Reaction mechanisms and kinetics of the synthesis and decomposition of lithium metazirconate through solid-state reaction. *J. Eur. Ceram. Soc.* **2004**, *24* (8), 2433–2443.

(15) Ida, J.; Xiong, R. T.; Lin, Y. S. Synthesis and CO$_2$ sorption properties of pure and modified lithium zirconate. *Sep. Purif. Technol.* **2004**, *36* (1), 41–51.

(16) Xiong, R. T.; Ida, J.; Lin, Y. S. Kinetics of carbon dioxide sorption on potassium-doped lithium zirconate. *Chem. Eng. Sci.* **2003**, *58* (19), 4377–4385.

(17) Zhao, T. J.; Ochoa-Fernandez, E.; Ronning, M.; Chen, D. Preparation and high-temperature CO$_2$ capture properties of nanocrystalline Na$_2$ZrO$_3$. *Chem. Mater.* **2007**, *19* (13), 3294–3301.

(18) Ochoa-Fernandez, E.; Ronning, M.; Grande, T.; Chen, D. Synthesis and CO$_2$ capture properties of nanocrystalline lithium zirconate. *Chem. Mater.* **2006**, *18* (25), 6037–6046.

(19) Han, C.; Harrison, D. P. Simultaneous shift reaction and carbon dioxide separation for the direct production of hydrogen. *Chem. Eng. Sci.* **1994**, *49* (24B), 5875–5883.

(20) Martavaltzi, C. S.; Lemonidou, A. A. Development of new CaO based sorbent materials for CO$_2$ removal at high temperature. *Microporous Mesoporous Mater.* **2008**, *110* (1), 119.

(21) Kuramoto, K.; Fujimoto, S.; Morita, A.; Shibano, S.; Suzuki, Y.; Hatano, H.; Lin, S. Y.; Harada, M.; Takarada, T. Repetitive carbonation–calcination reactions of Ca-based sorbents for efficient CO$_2$ sorption at elevated temperatures and pressures. *Ind. Eng. Chem. Res.* **2003**, *42* (5), 975–981.

(22) Yong, Z.; Mata, V.; Rodrigues, A. E. Adsorption of carbon dioxide on basic alumina at high temperatures. *J. Chem. Eng. Data* **2000**, *45* (6), 1093–1095.

(23) Yong, Z.; Mata, V. G.; Rodrigues, A. E. Adsorption of carbon dioxide on chemically modified high surface area carbon-based adsorbents at high temperature. *Adsorption* **2001**, *7* (1), 41–50.

(24) Kapoor, A.; Krishnamurthy, K. R.; Shirley, A. Kinetic separation of carbon dioxide from hydrocarbons using carbon molecular sieve. *Gas Sep. Purif.* **1993**, *7* (4), 259–263.

(25) Song, H. K.; Lee, K. H. Adsorption of carbon dioxide on chemically modified carbon adsorbents. *Sep. Sci. Technol.* **1998**, *33* (13), 2039–2057.

(26) Ding, Y.; Alpay, E. Equilibria and kinetics of CO$_2$ adsorption on hydrotalcite adsorbent. *Chem. Eng. Sci.* **2000**, *55* (17), 3461–3474.

(27) Ding, Y.; Alpay, E. Adsorption-enhanced steam-methane reforming. *Chem. Eng. Sci.* **2000**, *55* (18), 3929–3940.

(28) Ding, Y.; Alpay, E. High temperature recovery of CO$_2$ from flue cases using hydrotalcite adsorbent. *Process Saf. Environ. Prot.* **2001**, *79* (B1), 45–51.

(29) Nataraj, S.; Carvill, B. T.; Hufton, J. R.; Mayorga, S. G.; Gaffney, T. R.; Brozozowski, J. R. Materials selectivity adsorbing CO$_2$ from CO$_2$ containing streams. EP Patent No. 1006079A1, 2000.

(30) Winter, F.; Wolters, M.; van Dillen, A. J.; de Jong, K. P. A hydrotalcite-based catalyst system for the single-stage liquid-phase synthesis of MIBK. *Appl. Catal. A* **2006**, *307* (2), 231–238.

(31) Winter, F.; van Dillen, A. J.; de Jong, K. P. Supported hydrotalcites as highly active solid base catalysts. *Chem. Commun.* **2005**, (31), 3977–3979.

(32) Winter, F.; Koot, V.; van Dillen, A. J.; Geus, J. W.; de Jong, K. P. Hydrotalcites supported on carbon nanofibers as solid base catalysts for the synthesis of MlBK. *J. Catal.* **2005**, *236* (1), 91–100.

(33) Angelescu, E.; Pavel, O. D.; Birjega, R.; Zavoianu, R.; Costentin, G.; Che, M. Solid base catalysts obtained from hydrotalcite precursors, for

Knoevenagel synthesis of cinamic acid and coumarin derivatives. *Appl. Catal. A* **2006**, *308*, 13–18.

(34) Veldurthy, B.; Clacens, J. M.; Figueras, F. Magnesium-lanthanum mixed metal oxide: A strong solid base for the Michael addition reaction. *Adv. Synth. Catal.* **2005**, *347* (6), 767–771.

(35) Bontchev, R. P.; Liu, S.; Krumhansl, J. L.; Voigt, J.; Nenoff, T. M. Synthesis, characterization, and ion exchange properties of hydrotalcite $Mg_6Al_2(OH)_{16}(A)_x(A')_{2-x} \cdot 4H_2O$ (A, A′ = Cl^-, Br^-, I^-, and NO_3^-, $2 \geq x \geq 0$) derivatives. *Chem. Mater.* **2003**, *15* (19), 3669–3675.

(36) Costantino, U.; Coletti, N.; Nocchetti, M.; Aloisi, G. G.; Elisei, F. Anion exchange of methyl orange into Zn−Al synthetic hydrotalcite and photophysical characterization of the intercalates obtained. *Langmuir* **1999**, *15* (13), 4454–4460.

(37) Mohanambe, L.; Vasudevan, S. Anionic clays containing anti-inflammatory drug molecules: Comparison of molecular dynamics simulation and measurements. *J. Phys. Chem. B* **2005**, *109* (32), 15651–15658.

(38) Roelofs, J.; Lensveld, D. J.; van Dillen, A. J.; de Jong, K. P. On the structure of activated hydrotalcites as solid base catalysts for liquid-phase aldol condensation. *J. Catal.* **2001**, *203* (1), 184–191.

(39) Ogawa, M.; Kaiho, H. Homogeneous precipitation of uniform hydrotalcite particles. *Langmuir* **2002**, *18* (11), 4240–4242.

(40) van Dillen, A. J.; Geus, J. W.; L.A.M., H.; van der Meijden, J. *Proc. Int. Congr. Catal., 6th* **1977**, 677.

(41) Toebes, M. L.; van Heeswijk, E. M. P.; Bitter, J. H.; van Dillen, A. J.; de Jong, K. P. The influence of oxidation on the texture and the number of oxygen-containing surface groups of carbon nanofibers. *Carbon* **2004**, *42* (2), 307–315.

(42) Winter, F.; Bezemer, G. L.; van der Spek, C.; Meeldijk, J. D.; van Dillen, A. J.; Geus, J. W.; de Jong, K. P. TEM and XPS studies to reveal the presence of cobalt and palladium particles in the inner core of carbon nanofibers. *Carbon* **2005**, *43* (2), 327–332.

(43) Cavani, F.; Trifiro, F.; Vaccari, A. Hydrotalcite-type anionic clays: Preparation, properties and applications. *Catal. Today* **1991**, *11* (2), 173.

(44) Winter, F. Hydrotalcite-Based Catalysts for the Synthesis of Methyl Isobutyl Ketone. Ph.D. Thesis, Utrecht University, Utrecht, The Netherlands, 2006.

(45) Costantino, U.; Marmottini, F.; Nocchetti, M.; Vivani, R. New synthetic routes to hydrotalcite-like compounds−Characterisation and properties of the obtained materials. *Eur. J. Inorg. Chem.* **1998**, (10), 1439–1446.

(46) Kovanda, F.; Kolousek, D.; Cilova, Z.; Hulinsky, V. Crystallization of synthetic hydrotalcite under hydrothermal conditions. *Appl. Clay Sci.* **2005**, *28* (1−4), 101–109.

(47) Kim, S.-N.; Son, W.-J.; Choi, J.-S.; Ahn, W.-S. CO_2 adsorption using amine-functionalized mesoporous silica prepared via anionic surfac-tant-mediated synthesis. *Microporous Mesoporous Mater.* **2008**, *115* (3), 497–503.

(48) Bailly, M.-L.; Chizallet, C.; Costentin, G.; Krafft, J.-M.; Lauron-Pernot, H.; Che, M. A spectroscopy and catalysis study of the nature of

active sites of MgO catalysts: Thermodynamic Brønsted basicity versus reactivity of basic sites. *J. Catal.* **2005**, *235* (2), 413–422.

(49) Mario Chiesa, E. G. Carbon Dioxide Activation by Surface Excess Electrons: An EPR Study of the CO_2^- Radical Ion Adsorbed on the Surface of MgO. *Chem.−Eur. J.* **2007**, *13* (4), 1261–1267.

(50) Fishel, C. T.; Davis, R. J. Use of catalytic reactions to probe Mg−Al mixed oxide surfaces. *Catal. Lett.* **1994**, *25* (1), 87–95.

(51) Schneider, W. F. Qualitative differences in the adsorption chemistry of acidic (CO_2, SO_x) and Amphiphilic (NO_x) species on the alkaline earth oxides. *J. Phys. Chem. B* **2004**, *108* (1), 273–282.

(52) Florez, E.; Fuentealba, P.; Mondragon, F. Chemical reactivity of oxygen vacancies on the MgO surface: Reactions with CO_2, NO_2 and metals. *Catal. Today* **2008**, *133*, 216–222.

(53) Pacchioni, G. Physisorbed and Chemisorbed CO_2 at Surface and Step Sites of the MgO(100) Surface. *Surf. Sci.* **1993**, *281* (1−2), 207–219.

(54) Meixner, D. L.; Arthur, D. A.; George, S. M. Kinetics of desorption, adsorption, and surface diffusion of CO_2 on MgO(100). *Surf. Sci.* **1992**, *261* (1−3), 141–154.

(55) Daub, C. D.; Patey, G. N.; Jack, D. B.; Sallabi, A. K. Monte Carlo simulations of the adsorption of CO_2 on the MgO(100) surface. *J. Chem. Phys.* **2006**, *124* (11), 114706.

(56) Preda, G.; Pacchioni, G.; Chiesa, M.; Giamello, E. Formation of CO_2^- Radical Anions from CO_2 Adsorption on an Electron-Rich MgO Surface: A Combined ab Initio and Pulse EPR Study. *J. Phys. Chem. C* **2008**, *112* (49), 19568–19576.

(57) McKenzie, A. L.; Fishel, C. T.; Davis, R. J. Investigation of the Surface Structure and Basic Properties of Calcined Hydrotalcites. *J. Catal.* **1992**, *138* (2), 547–561.

(58) Virnovskaia, A.; Morandi, S.; Rytter, E.; Ghiotti, G.; Olsbye, U. Characterization of Pt,Sn/Mg(Al)O Catalysts for Light Alkane Dehydro-genation by FT-IR Spectroscopy and Catalytic Measurements. *J. Phys. Chem. C* **2007**, *111* (40), 14732–14742.

(59) Karlsen, E. J.; Nygren, M. A.; Pettersson, L. G. M. Comparative study on structures and energetics of NO_x, SO_x, and CO_x adsorption on alkaline-earth-metal oxides. *J. Phys. Chem. B* **2003**, *107* (31), 7795–7802.

(60) Jensen, M. B.; Pettersson, L. G. M.; Swang, O.; Olsbye, U. CO_2 sorption on MgO and CaO surfaces: A comparative quantum chemical cluster study. *J. Phys. Chem. B* **2005**, *109* (35), 16774–16781.

(61) Chimentao, R. J.; Abello, S.; Medina, F.; Llorca, J.; Sueiras, J. E.; Cesteros, Y.; Salagre, P. Defect-induced strategies for the creation of highly active hydrotalcites in base-catalyzed reactions. *J. Catal.* **2007**, *252* (2), 249–257.

(62) Climent, M. J.; Corma, A.; Iborra, S.; Epping, K.; Velty, A. Increasing the basicity and catalytic activity of hydrotalcites by different synthesis procedures. *J. Catal.* **2004**, *225* (2), 316–326.